Available free online at www.medjchem.com

Mediterranean Journal of Chemistry **2018**, 6(6), 255-266

Electrocatalytic properties of hydroxyapatite thin films electrodeposited on stainless steel substrates

Ahmed Chennah [1], Yassine Naciri [1], Hassan Ait Ahsaine [1], Aziz Taoufyq [1], Bahcine Bakiz [1], Lahcen Bazzi [1], Frédéric Guinneton [2], Jean-Raymond Gavarri [2,*] and Abdeljalil Benlhachemi [1]

[1] Laboratoire Matériaux & Environnement (LME), Université IBN ZOHR, Agadir, Morocco

[2] Institut Matériaux Microélectronique & Nanosciences de Provence (IM2NP), UMR CNRS 7334, Université de Toulon, France

Abstract: In this work, we have investigated the structural, microstructural, and electrocatalytic properties of hydroxyapatite (HAp) thin films. The HAp films were electrodeposited on stainless-steel (SS) substrates by chronopotentiometry mode from an electrolytic solution. The HAp films were characterized by X-ray diffraction (XRD), scanning electron microscopy (SEM) and X-ray energy dispersion spectroscopy (EDS). The electrodeposition and electrochemical processes of the hydroxyapatite (HAp) phase were studied by cyclic voltammetry. This HAp/SS system acting as an anode was used for the first time to electrodegrade Rhodamine B (RhB) in aqueous solutions. To follow the degradation kinetics, we used UV-visible spectroscopy. Several parameters such as the current density and the initial concentration of electrolytic solution were determined to optimize the electrodegradation of RhB. The decrease of RhB concentration followed pseudo-first order kinetics law. The rate of RhB degradation in presence of HAp/SS electrode can reach interesting high performance, depending on the electrocatalysis experimental conditions.

Key-words: electrodeposition; hydroxyapatite; chronopotentiometry; electrodegradation; Rhodamine B.

Introduction

The phosphates are largely used in many domains, firstly, in the biomaterial domain, such as the bone filling materials or the prosthetic coating, because of their specific responses in a physiological medium [1-3]. Secondly, they are known in the domain of corrosion inhibition [4]. Thirdly, these materials are tested as photocatalysts for the degradation of organic pollutants like phenol [5] and dyes such as methylene blue (BM) [6].

Several technics such as plasma torch, pulverization, electrostatic spray, sol-gel process and electrodeposition technics [7-11] are used for calcium phosphate coatings. The majority of works published in the domain of organic pollutant electrodegradation focuses on electrodeposition since this approach offers performant results with low cost [12,13].

Many electrocatalysts without noble metals are used as active anodes, at a fairly advanced stage. The increasing performance of these materials is clearly observed through the first studies that have shown their remarkable potentiality. Moreover, nowadays, the most promising materials are based on transition metals (Fe, Co, Mo, Ag…) [14,15]. and phosphate-based compounds [14,16]. For example, silver phosphate electrodes showed strong electrocatalytic activity [17-19]. Molybdenum phosphate electrodes showed a very interesting behavior for the reduction of the oxygen in aqueous medium at acidic pH [9]. Despite the promising properties of this type of materials, there is a lack of information on their electrocatalytic behaviors, which encouraged us to work on the development of phosphate-based electrodes for the electrodegradation of Rhodamine B (RhB).

Rhodamine B (RhB) is one of the colorants belonging to the xanthene group currently used in textile industry. However, its toxicity and the consequences on environment and health were the objects of many scientific studies [21,22,34] mainly in the case of photocatalytic degradation of RhB particles in presence of photocatalysts in aqueous media. Depending on photocatalysts, the mechanism of degradation of this standard pollutant can be diversified, incomplete with

**Corresponding author: Jean-Raymond Gavarri*
Email address: gavarri.jr@univ-tln.fr
DOI: http://dx.doi.org/10.13171/mjc66/01712241118-gavarri

Received October 13, 2017
Accepted, October 30, 2017
Published December 24, 2017

residual intermediates or complete by the production of CO_2 and H_2O.

For this reason, we developed systematic electro-syntheses of compact films based on hydroxyapatite, electrodeposited on metal substrates of stainless-steel. In the past, the RhB pollutant was electrodegraded by different electrode materials used as anodes, such as lead dioxide, cerium doped lead oxide Ce-PbO_2 [20] and zinc tungstate $ZnWO_4$ [21].

Herein, we report the electrodeposition procedure of calcium phosphate on stainless-steel substrates to constitute HAp/stainless-steel specific anodes, followed by the electrodegradation of RhB by HAp/stainless-steel electrodes in aqueous media. The as-prepared Hap films have been characterized by X-ray diffraction (XRD), scanning electron microscopy (SEM) and X-ray energy dispersion spectroscopy (EDS).

Materials and method

Materials

PGP 201 Radiometer Copenhagen Voltalab TM potentiostat /galvanostat was used to perform the potentiostatic deposition. The working electrodes were made from 1.5 mm thick stainless-steel foils, cut in circular round plates of 2.5 cm in diameter, and on which the thin films of HAp were electrodeposited. The stainless steel used for these substrates was a specific reference steel 316 (17% Cr, 12% Ni, 2% Mo).

The surfaces of the substrates were previously polished with SiC abrasive paper (grit from P320 to P1200), followed by rinsing with acetone and ethanol many times. A plastic seal was used to cover the surface of the substrate and leave an area of 1 cm^2.

Process of electrodeposition

All chemicals are from Sigma Aldrich with a high analytical purity. The electrolyte was prepared by dissolving calcium nitrate tetrahydrate ($Ca(NO_3)_2.4H_2O$) and ammonium dihydrogen phosphate ($NH_4H_2PO_4$). A set of solutions were used for calcium phosphate deposition (Table 1). The molar fractions of $Ca(NO_3)_2.4H_2O$ and $NH_4H_2PO_4$ were taken to ensure that the molar ratios Ca/P were kept constant at approximately 1.67 (theoretical ratio of 5/3), equal to that of the stoichiometric composition of the hydroxyapatite $Ca_{10}(PO_4)_6(OH)_2$. The initial pH of the electrolyte is equal to 4.45 at 25 °C.

Table 1. Variation of deposited HAp film weight with precursor concentrations.

Solution	$Ca(NO_3)_2,4H_2O$ (M)	$NH_4H_2PO_4$ (M)	Deposit mass on stainless steel (mg)	Calculated deposit thickness (µm)	Deposit rate ($\mu m.min^{-1}$)
S1	$1.5\ 10^{-2}$	$0.9\ 10^{-2}$	1.4 (0.1)	0.45	0.030
S2	$2\ 10^{-2}$	$1.2\ 10^{-2}$	1.7 (0.1)	0.55	0.037
S3 (*)	$3\ 10^{-2}$	$1.8\ 10^{-2}$	2.5 (0.15)	0.8 to 1.6 (*)	0.053 to 0.11
S4	$4.2\ 10^{-2}$	$2.5\ 10^{-2}$	1.8 (0.1)	0.58	0.068
(*) Note: porous sample with estimated density					

The thin films of Hap calcium phosphate were electrodeposited by galvanostatic mode, using a conventional three-electrode cell illustrated in Fig. 1.

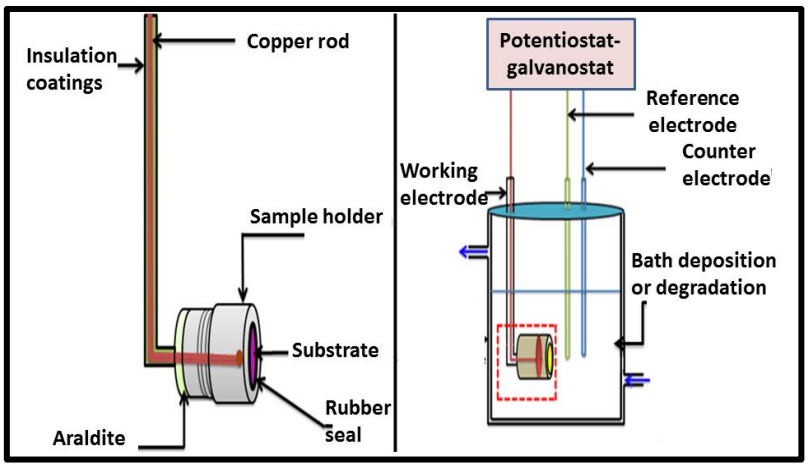

Figure 1. Schematic representation of the electrodegradation device.

Saturated calomel electrode (Hg / Hg_2Cl_2 / KCl) (242 mV relative to the standard hydrogen electrode at room temperature) was used as reference electrode. A platinum plate was used as a counter electrode, and the working electrode was the stainless-steel substrate, described just above. An evaluation of thicknesses was carried out using the density of crystalline HAp ($\mu_{(HAp)}$ = 3.08 $g.cm^{-3}$) as a first approach: for the S1 and S2 samples, due to the continuity of the layers observed from SEM analyses, this calculation could be justified. However, for the S3 sample, the apparent density is weaker (not far from 50%), which could involve a strong deviation of this evaluation. The extreme limits of thickness for this sample are given in Table 1, only as a first indication.

The decrease of HAp mass after the deposit was verified by preliminary results allowing testing the device: the present results confirmed the previous works by authors [22].

The electroplating conditions were as follows:

- Precursor concentrations [$Ca(NO_3)_2.4H_2O$] = 3 10^{-2} M; [$NH_4H_2PO_4$] = 1.8 10^{-2} M
- Temperature of deposit: 60 °C
- Galvanostatic mode
- Three electrodes: ECS as a reference, platinum plate as a counter electrode and SS plate as working electrode.
- Current density: - 10 $mA.cm^{-2}$
- pH of electrolytic bath : 4.4
- Deposit bath volume: 100 mL; Deposit time: 15 min

Structural and microstructural characterizations of deposits

The X-Ray diffraction (XRD) patterns were collected from an EMPYREAN PANALYTICAL diffractometer operating at 45 kV/35 mA, using CuKα radiation with Ni filter. The wavelength of the radiation used to record the diffraction data was the doublet 1.540-1.544 Å. The thin layers of calcium phosphate were analyzed by Grazing Incidence X-Ray Diffraction (GIXRD). The lower the angle of incidence, the higher the depth of penetration is low: therefore, the diffraction data obtained on the diffractograms will concern the coating more than the substrate. In contrast to the θ-2θ configuration in which the sample holder performs a rotational movement (dθ/dt) coordinated with the detector (d2θ/dt), the GIXRD configuration is performed at a fixed angle (θ = α) for the sample, and a variable angle (2θ) for the detector. In this study, the angle α was optimized experimentally by testing several angles from 0.2° to 5°. As the best result was obtained with an angle of 3°, the diffraction profiles were recorded for all samples with the same grazing incidence α = 3°, over an angular range from 10° to 80° (2θ) with a step of 0.01° and an angular velocity of 0.06° s^{-1}.

The average size of the crystallites was calculated using Scherrer method, by applying the following equation:

$$\mathbf{D = (K.\ \lambda) / (\Delta(2\theta).\ \cos\ \theta)}$$

D: Average crystallite size in nm,
K: Shape factor (K = 0.9 in the case of Gaussian profiles),
λ: Wavelength of incident radiation in (nm),
θ: Bragg angle of diffraction in degree,
Δ(2θ): widening of the Bragg peak due to the size effect expressed in radians $(\Delta(2\theta))^2 = (FWHM)^2 - \omega^2$
where FWHM is the total observed full width at half maximum of Bragg peak, ω is the corresponding FWHM of a well crystallized standard (presently a well crystallized standard powder of HAp).

The morphology was characterized by scanning electron microscopy (SEM) coupled with chemical element analysis. The device used was a ZEISS SUPRA 40VP COLUMN GEMINI coupled with an Energy Dispersive X-rays Spectroscopy (EDXS) analyzer from Oxford Instruments (X-MAX 20 mm^2), allowing determining the local elemental composition of a sample with a maximum resolution of 1 µm, under voltages ranging from 10 to 25 kV.

Preparation of Rhodamine B solution

As shown in Fig. 1, RhB electrodegradation by electrocatalysis was performed in a glass electrochemical cell containing 100 mL of the pollutant (5 $mg.L^{-1}$ of RhB). The initial supporting electrolyte was a solution of 0.1M Na_2SO_4 and 0.01M NaCl. The anode consisted of the stainless-steel plate coated with hydroxyapatite HAp. The cathode was as platinum sheet positioned vertically and parallel to the working electrode, at a distance of 1.5 cm. The saturated calomel electrode (ECS) was used as reference electrode. We should note that the electrodegradation was carried out at room temperature (25 °C).

The determination of degradation rate was performed using a UV-visible spectrophotometer 2300 as a function of time. Samples of the stock solution were taken at regular time intervals and their UV-visible absorption spectra were recorded: the 554nm absorption band characteristic of RhB was chosen to monitor the change in RhB concentration as a function of time.

Results and Discussion

Effect of precursor concentration in HAp electrodeposition.

The mass variation of the electrodeposited Hap calcium phosphate with the precursor concentrations is shown in Table 1. Four solutions (S1 to S4) were prepared with increasing

concentrations of precursors ($10Ca(NO_3)_2.4H_2O$ + $6NH_4H_2PO_4$). The weights of the films were determined by measuring the mass variation of the substrate, before and after deposition, using a highprecision balance (with relative uncertainties of 5 to 8 w%).

These weights of films increased from S1 to S3 solutions. In the case of solution S4, a decrease of weight was observed. The increasing weight from S1 to S3 corresponds to the deposition rate of the film associated with increasing population of reagents at the surface of substrates.

The reactions on the surface of working electrode would generate increasing reduction of protons species ($H_2PO_4^-$➔ HPO_4^{2-}➔ PO_4^{3-} ions, with $2H^+ + 2e^-$➔H_2), increasing formation of OH^- and PO_4^{3-} ionic species, directly associated with the increase of the current density at the interface electrode/solution. When the precursor concentrations reach a certain level in the case of S4 solution, the $H_2PO_4^-$ species would be in excess, the diffusion of the ions OH^- and PO_4^{3-} from the surface of the electrode into the solution will be preponderant, which would cause a certain solubility of the phosphate based film and more precisely a decrease of the growth of phosphate film [22].

As observed by authors [23], ionic concentrations of solutions can play a prominent role in the composition of coatings: concentrations greater than 0.050 $mol.L^{-1}$ in calcium ions ($Ca(NO_3)_2.4H_2O$) and more than 0.030 $mol.L^{-1}$ in dihydrogen phosphate ions ($NH_4H_2PO_4$) would be favorable to the formation of brushite phase $CaHPO_4.2H_2O$ [23]. Obviously, the nature and concentration of the electrolyte play important roles in the deposition kinetics, which would condition the thickness of the coating. In our study, we found that the mass of calcium phosphate electrodeposited on stainless-steel substrate could be maximum for the concentrations 3.10^{-2} mol. L^{-1} in $Ca(NO_3)_2.4H_2O$ and $1.8.10^{-2}$ $mol.L^{-1}$ in $NH_4H_2PO_4$ corresponding to sample S3 (see Table 1). The same result was found by Thanh and al.[22] This indicates that a too high concentration of dihydrogen phosphate ions would disadvantage the formation of hydroxide ions OH^-, which would lead to the increase of the pH in the vicinity of the cathode [24]. For these reasons, the solution S3 was considered as being the optimal solution.

Effect of deposition bath temperature

X-ray diffraction study.

The hydroxyapatite (HAp) crystallizes in hexagonal system, with space group $P6_3/m$: the cell parameters are a = b= 9.41 Å and c = 6.88 Å (γ = 120°) with two formula units per cell. Since the electrodeposited phase on this stainless-steel substrate was not well crystallized, the temperature of the electrolyte was varied from 25 °C to 60 °C (Fig.2). Fig. 2 shows observed Bragg peaks characterized by intensities increasing with increasing temperature while FWHM's decreased with this increasing temperature.

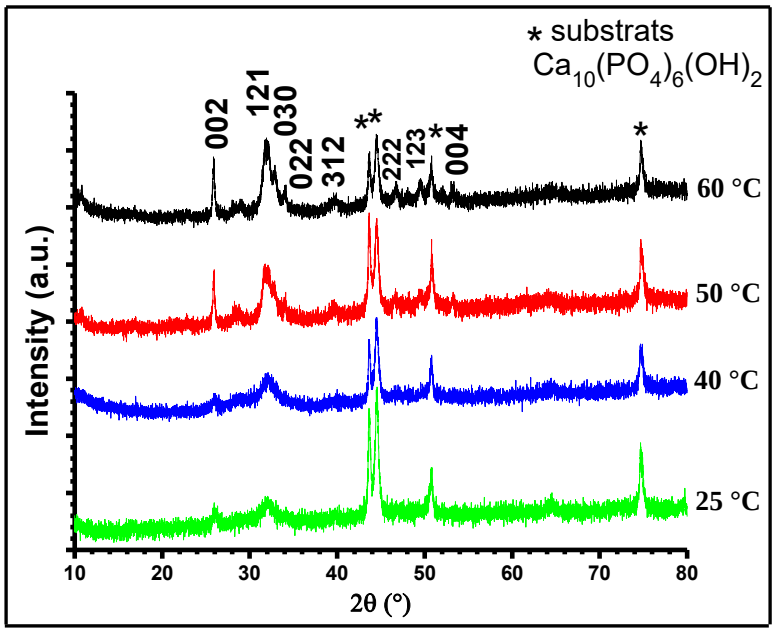

Figure 2. X-ray diffraction patterns of thin films electrodeposited on stainless-steel substrate, at 25 °C, 40 °C, 50 °C, and 60 °C, ($[Ca(NO_3)_2.4H_2O] = 3\ 10^{-2}$, $[NH_4H_2PO_4] = 1.8\ 10^{-2}$).

In the diffraction pattern obtained from solution S3 at 60°C, we observe a series of Bragg peaks with (hkl) Miller indices characteristic of HAp: (002) at 25.5° 2θ, (121) (030), (022) close to 32° 2θ, (312) at 41° 2θ, (222) at 47° 2θ, (123) at 49.5° 2θ, (004) at 52° 2θ. At 50 °C, the same Bragg peaks can be observed with weaker intensities. At 40 °C, the Bragg peaks present

weak intensities and large profiles. In general, it appears that, as temperature increases, the full widths at half maximum (FWHM) of the Bragg peaks decrease. This means that the degree of crystallization increases. The specific Bragg peak (002) is particularly thin and characteristic of a large crystal dimension along the c axis of the HAp hexagonal structure: this will be confirmed by the SEM analyses just below, where long needles (or wires) are observed in samples obtained at 60 °C. This was quantified by determining the crystallite size effects from the Scherrer method. With bath temperatures of 50 °C and 60 °C, the average crystallite sizes in the c axis direction of the hexagonal crystal structure were found to be greater than 200 nm, while the average sizes in directions perpendicular to this c axis were found to be of about 70±10 and 90±11 nm, respectively. With bath temperatures of 25 °C and 40 °C, the average crystallite sizes were found to be weaker (of about 80 nm in the c axis direction and 50 nm in the direction perpendicular to this c axis, respectively). Given the experimental uncertainties associated with this GIXRD configuration, it was not possible to evaluate possible crystal lattice distortions contributing to the widening of the Bragg peaks.

Study of the morphology

Fig. 3 represents the observed morphologies of the electrodeposited samples at 60 °C (3a) and 25 °C (3b).

The SEM images reveal that the morphology of HAp layers deposited at 60 °C is characterized by agglomeration of needles characterized by lengths of several hundred nanometers and diameters of a few nanometers, as shown in Fig. 3a.

This morphology could correspond to a fast crystal growth in the [002] directions of HAp hexagonal structure, in good agreement with the X-ray diffraction profiles (small FWHM of (002) Bragg peaks) discussed just above. The surface appears to be not very dense, due to this needle-like morphology that allows the formation of voids in needles agglomerates. The observed films constituted of needles present certain porosity, as it can be seen in Fig. 3a. In Fig. 3b, in the case of samples electrodeposited at 25 °C, compact agglomerations of spherical grains forming continuous surfaces, with sizes varying between 50 and 200 nanometers are observed. This change in grain sizes of Hap film as a function of the bath temperature is consistent with the crystallite sizes obtained by XRD analyses. In the rest of the text, the films obtained at 60 °C with solutions S3 will be noted S3-60.

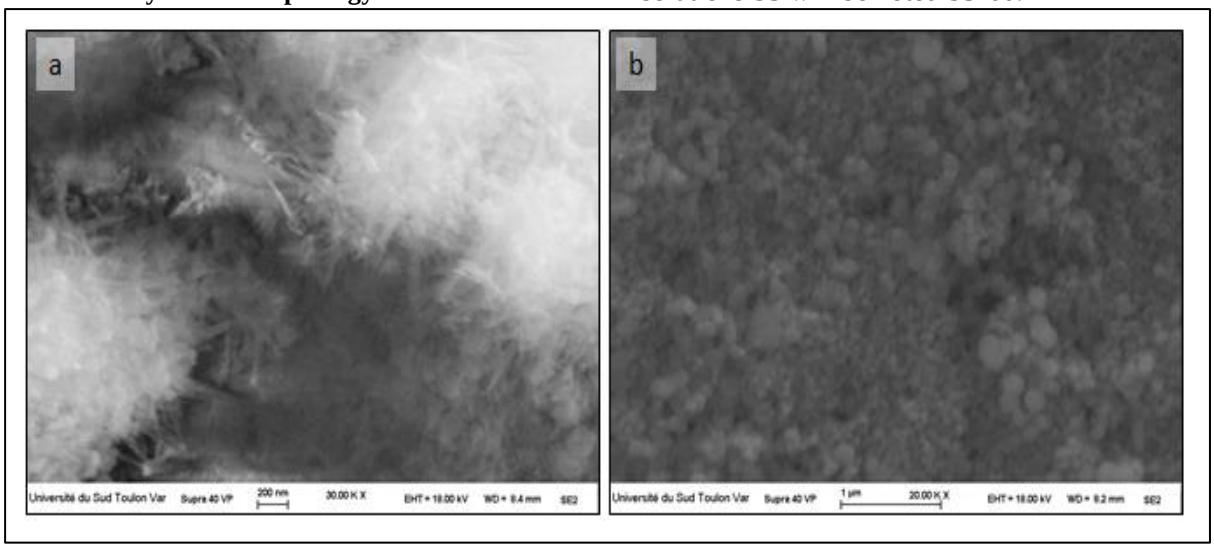

Figure 3. SEM photographs observed on deposits of hydroxyapatite obtained at various temperatures: (a) at 60 °C and (b) at 25 °C (b), on a stainless-steel substrate.

Characterization of the composition

The chemical composition was determined using energy-dispersive X-ray spectroscopy coupled with SEM. Fig. 4 shows the results of an overall analysis obtained from the electrodeposited HAp calcium phosphate on stainless-steel substrate, at 25 °C (Fig. 4a) and 60 °C (Fig. 4b). The thin layers are constituted of grains of different sizes containing phosphorus, calcium, and oxygen. The overall analysis agrees with the XRD phase determination: the theoretical Ca/P ratios of the films electrodeposited at 25 °C and 60 °C were found equal to 1.60 ± 0.04 and 1.66 or 1.64 ± 0.04 (Fig. 4b), respectively. The small deviations from the theoretical ratio of 1.67 could be ascribed first to experimental errors, and then to differences in porosity of films.

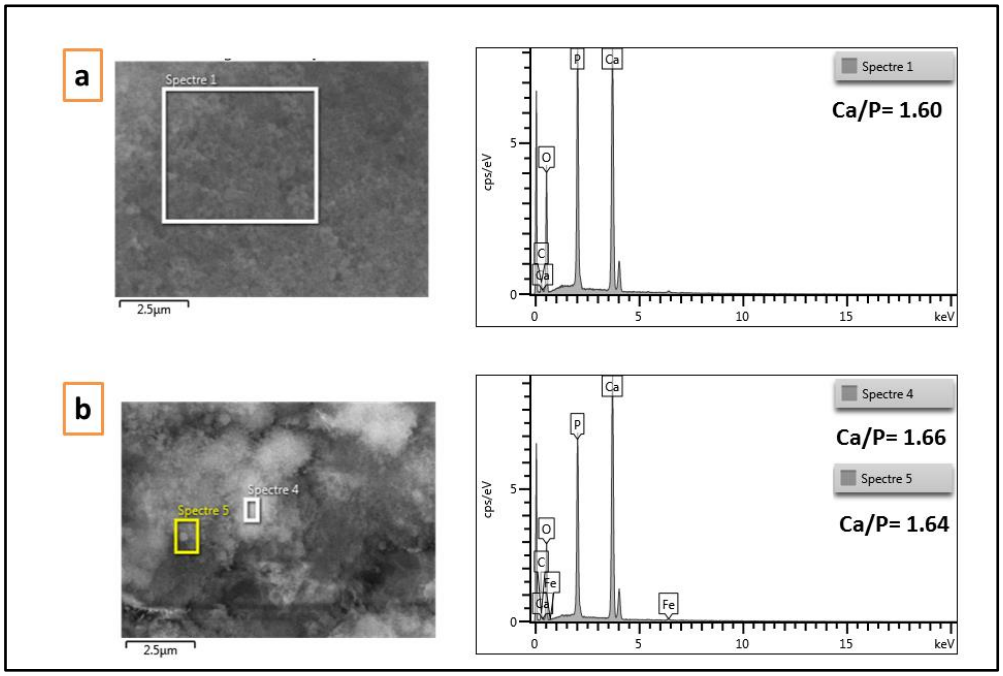

Figure 4. Energy-dispersive X-ray spectroscopy (EDS) analysis of phosphocalcic coating electrodeposited on the stainless-steel substrate (a) 25 °C and (b) 60 °C.

Electrochemical characterization (S3-60 HAp films)

Study of the solution by cyclic voltamperometry.

The polarization curve obtained from solution S3 (3.10^{-2} mol.L^{-1} in $Ca(NO_3)_2$,$4H_2O$ + $1.8\ 10^{-2}$ mol.L^{-1} in $NH_4H_2PO_4$) with stainless-steel as working electrode is shown in Fig.5. A cathodic scan between -0.3 V and -2 V (/SCE electrode), with a scanning speed of 50 mV/s, was performed in this solution. Generally, the voltammetric scan allows identifying the oxidation-reduction process, possibly undergone by the system. In this Figure, the reduction cathodic peak of phosphate ions $H_2PO_4^-$ on the stainless-steel substrate is located close to a voltage of -1 V and a current density of -8 mA.cm^{-2}. For applied voltages comprised between -0.6 V and -0.3 V, the anodic current would be mainly supplied by the oxidation of water on the surface of the working electrode (reaction (1)). For voltages less than - 0.6 V, a cathodic current was observed (reduction of water: reactions 2 and 3), which corresponded to different reactions on the surface of the substrate.

The anodic oxidation of water [Reaction (1)], according to Kuo et al.[25], should be as follows:

$$2\ H_2O \rightarrow O_2 + 4\ H^+ + 4\ e^- \quad (1)$$

The cathodic reduction is accompanied by dihydrogen H_2 bubbles cleared from the surface of the cathode:

$$2\ H_2O + 2e^- \rightarrow H_2 + 2OH^- \quad (2)$$

Since the pH of the solution is acidic (4.4) the proton reduction reaction is predominant [Reaction (3)]:

$$2\ H^+ + 2e^- \rightarrow H_2 \quad (3)$$

When the electrolyte has just been prepared, its pH has an average value comprised between 4 and 5, value for which the dihydrogen phosphate ions $H_2PO_4^-$ are the preponderant species. If the pH value at the interface of the cathode is between 7 and 12, the hydrogen phosphate ions HPO_4^{2-} then become the majority [9] :

$$H_2PO_4^- + OH^- \rightarrow HPO_4^{2-} + H_2O \quad (4)$$

For a pH higher than 12, the phosphate ions PO_4^{3-} become the majority [9,26] :

$$HPO_4^{2-} + OH^- \rightarrow PO_4^{3-} + H_2O \quad (5)$$

Reactions (4) and (5) mean that a saturation of phosphate ions is reached at the electrode/electrolyte interface, which causes the precipitation of phosphocalcic phases for which the solubility product is generally moderate. According to the values of pH reached near the cathode, various compounds can precipitate [9,26,27] as shown just below.

Precipitation of brushite:

$$Ca^{2+} + HPO_4^{2-} + 2\ H_2O \rightarrow CaHPO_4,\ 2\ H_2O \quad (6)$$

Precipitation of hydroxyapatite:

$$10\ Ca^{2+} + 6\ PO_4^{3-} + 2\ OH^- \rightarrow Ca_{10}(PO_4)_6(OH)_2 \quad (7)$$

In reaction (7), the phosphate ions PO_4^{3-} interacting with the Ca^{2+} ions form a coating of hydroxyapatite $Ca_{10}(PO_4)_6(OH)_2$ on the stainless-steel substrate. This can be explained by the variation of pH in the vicinity of the working electrode. For stainless-steel substrate, the pH is greater than 12, which means that there is more OH^- at the interface. This result is in agreement, on the one hand, with the schema proposed by Lynn and Bonfield [28], and, on the other hand, with the curves of the cyclic voltammetry of Fig. 5.

On Fig.5, we observe a cathodic peak corresponding to the reduction of water (reaction (2)) giving rise to OH^- production at the electrode surface, followed by the reactions (4) (5) and finally (7) corresponding to the precipitation of HAp.

Water molecule H_2O can be oxidizing or reducing, and two redox properties can be classically expected depending on the medium. If we consider the redox potential expressed in standard conditions with ECS standard electrode:

$H^+ + e^- \rightarrow ½ H_2$ with pH = 4.4.

$E = E° + 0.06 \log[H^+] = - 0.244 – 0.06\ pH = - 0.244 – 0.264 = - 0.508$ V/ECS.

The observed signal ranges between - 0.8 V and – 1.1 V with a maximum for 1 V. This means that a supplementary cathodic current appears because of the precipitation of $Ca_{10}(PO_4)_6(OH)_2$ phase giving rise to acceleration of water reduction.

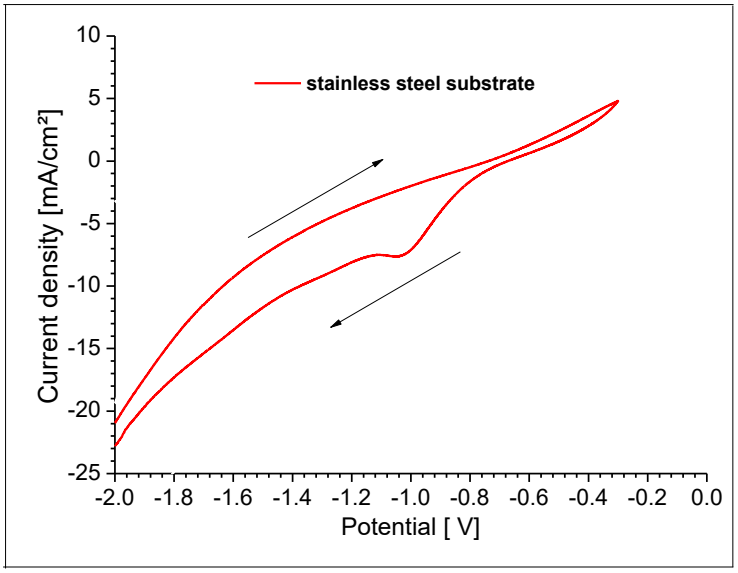

Figure 5. Cyclic voltamperometry of the solution containing 3.10^{-2} mol.L^{-1} of $Ca(NO_3)_2,4H_2O$ and 1.8 10^{-2} mol.L^{-1} of $NH_4H_2PO_4$. The scanning rate is 50 mV/s. The working electrode is stainless steel. Deposit bath temperature = 60 °C.

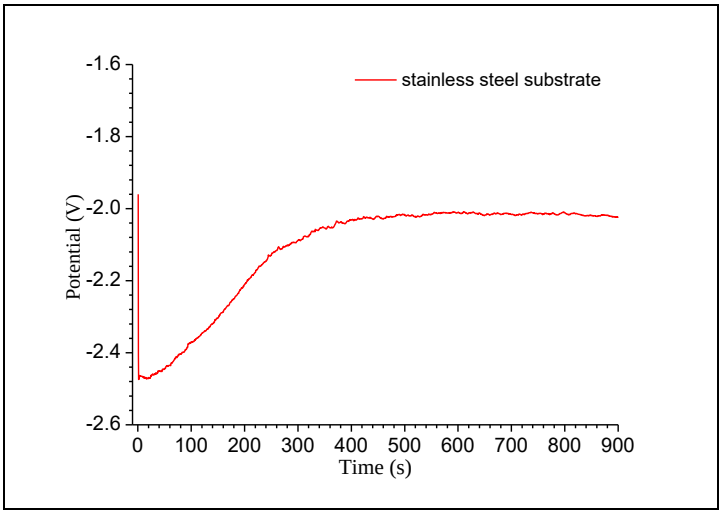

Figure 6. Chronopotentiometry curve obtained for j = -10 mA.cm^{-2}. Solution containing 3.10^{-2} mol.L^{-1} of $Ca(NO_3)_2,4H_2O$ and 1.8 10^{-2} mol.L^{-1} of $NH_4H_2PO_4$. The working electrode is stainless-steel (without any HAp deposit). Deposit bath temperature = 60 °C, deposit time = 15 min.

Study of the deposits by galvanostatic method.

The electrolytic deposit was carried out using PGP 201 Radiometer Copenhagen Voltalab, in galvanostatic mode. The galvanostatic methods are generally associated with low-cost electrical equipment, and beneficiate of operating simplicity. A current density of -10 mA.cm^{-2} was applied to the electrical circuit of the electrolytic cell. The temperature of the cell was maintained constant at 25 °C by a thermostat. Fig. 6 presents the variation of the potential relative to the saturated calomel electrode as a function of time (chronopotentiometry). When the current is applied, the potential decreases rapidly to about -2.5 V for 20 seconds, then gradually increases for 300 seconds to -2 V, and finally remains stable. A similar evolution was noted by Eliaz and al.[29] who attributed this evolution to the growth of phosphocalcic coating. The rapid decrease of the initial potential can be explained by the double layer charge. The increase of potential following this first stage could be ascribed to a one-dimensional crystal growth. At the end, the stability of the potential would indicate that the surface of the cathode would be no longer modified [29].

Figure 6 represents three deposit steps: (i) fast decrease during the first seconds corresponding to the electrical charge of the double layer; (ii) increase of potentially linked to the unidimensional growth of coating; (iii) finally, the stabilization of the potential close to 2V, corresponding to the invariance of the electrode surface [9].

Electrodegradation of Rhodamine B

To determine the electrocatalytic efficiency of the as-elaborated electrodes for the removal of contaminants in an aqueous medium, we have studied the electrocatalytic degradation of the RhB solution, by applying an electric current. Electrodes HAp/SS were the optimized ones S3-60 obtained (at 60 °C).

In the literature, two different approaches were developed for the electrocatalytic degradation of RhB, with two mechanisms involved: the direct mechanism leading to the degradation of RhB without any intermediate, and the indirect mechanism leading to a progressive degradation, with molecular intermediates.

Cyclic voltammetry.

The cyclic voltammetry for the three-electrode system registered between 0.5 V and 1.8 V is shown in Fig. 7. For the stainless steel electrode coated with hydroxyapatite (SS/HAp), we observed that the presence of Rhodamine B in the solution did not lead to the appearance of the characteristic peaks of degradation of this dye, which indicated that the direct transfer of electrons did not occur between the stainless-steel electrode and RhB, during the electrochemical process [30]. It was previously established that RhB degradation could be obtained via electrochemical oxidation mediated by oxidizing agents generated at the surface of the electrode by electrolysis: either by the radicals $HO^{\bullet}$ [20,31,32], and/or the active chloride Cl^{-} (indirect electrochemical oxidation) [30,33].

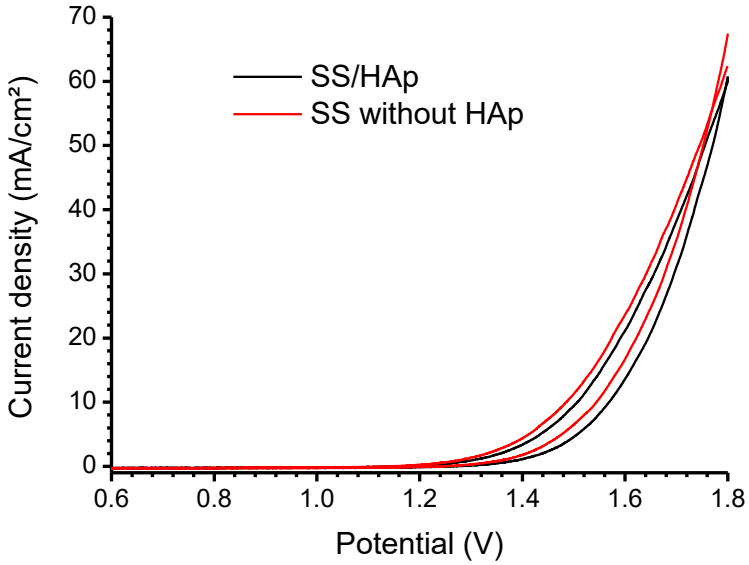

Figure 7. Cyclic voltammogram of calcium phosphate electrodeposited on the stainless-steel substrate (deposited in a bath of calcium nitrate tetrahydrate and ammonium dihydrogenphosphate for 15 minutes) in the presence and absence of 5 mg. L^{-1} of RhB (scanning rate: 50 mV.s^{-1}, Electrolyte support: 0.1 M of Na_2SO_4 and 0.01 M of NaCl).

The curves associated with the HAp/SS electrodes are quite similar to the ones associated with the SS electrodes. This shows that RhB present in the electrolyte cannot be degraded via electrons from the

HAp/SS system: in other terms, degradation of RhB requires the action of intermediate species (HO° and/or active Cl, see ref [20]), resulting from water electrolysis.

Standard experiments at fixed applied current density.

Standard experiments comparing SS electrode with SS/HAp electrode were performed at fixed applied current with initial concentrations C_0 of RhB. The variations of RhB concentrations C_t as a function of time t (in min) were determined from the intensities of the absorption band at 554 nm. The measurements were systematically performed in sets of three experiments. The variations of relative concentrations of Rh B (ratio C_t/C_0) as a function of reaction time t are shown in Fig. 8. It is clear that Rh B can be efficiently degraded using the S3-60 HAp film by applying a current density equal - 30 mA.cm^{-2}. Only 24% Rh B disappears from the solution with the SS electrode without HAp film. This lower degradation can be due to low adsorption capacity of RhB molecules on the SS electrode metallic surface, while a high adsorption capacity of these RhB molecules would be possible on the HAp/SS surface. This is consistent with the porous morphology of S3-60 films.

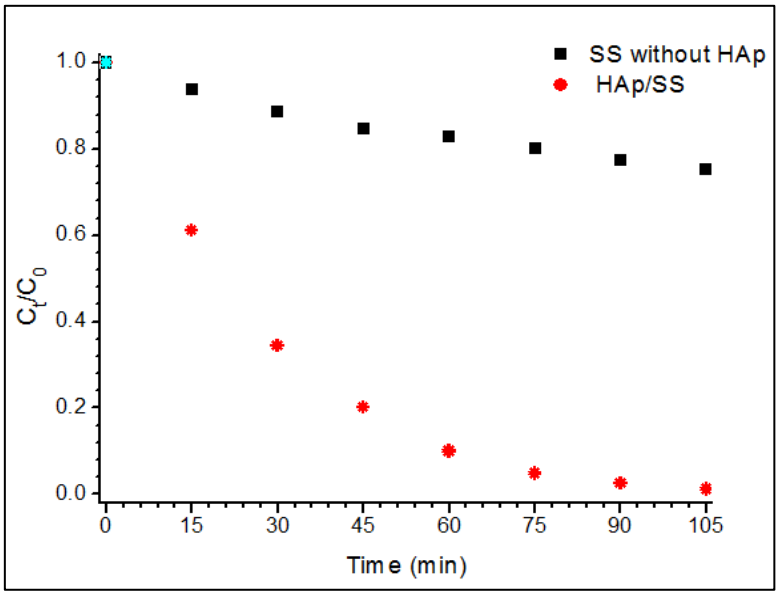

Figure 8. Degradation of RhB at fixed applied current density (-30 mA.cm-2). Variation of Ct/C0 concentration ratios for initial concentration of 5 mg. L^{-1} Rh.B. Top curve: with stainless steel (SS) electrode without HAp film. Bottom curve: with SS/HAp electrode. Temperature = 25 °C, pH = 6.4.

Effect of current density

It is well-known that the current density is a very important parameter governing the electrochemical degradation of organic pollutants. The electrochemical analyses were also performed by repeating experiments on the same sample to test the reproducibility of results and the stability of the samples.

Fig. 9a reports the ratios C_t / C_0, of the RhB concentrations at time t (C_t) on the initial RhB concentration C_0, under different current densities. An increase of current density between 5 and 30 mA.cm^{-2} led to a rapid degradation of the RhB. This was previously observed by authors [20,30] who showed that higher current densities could lead to a strong oxidant production by electrolysis. In our experiments, for time t = 105 min, the ratio C_t/C_0 decreases by 17% for a current density of 5 mA/cm^2, and 98% for a current density of 30 mA/cm^2.

Fig. 9b shows that the degradation mechanism of this dye could be described by a pseudo first order kinetics law (Langmuir-Hinshelwood model: d[RhB]/dt = -k[RhB]), under different current densities. The corresponding velocity constants are: k_5 = 0.0034 min^{-1}, k_{10} = 0.007 min^{-1}, k_{20} = 0.0176 min^{-1} and k_{30} = 0.0399 min^{-1} for current densities of 5 mA.cm^{-2}, 10 mA.cm^{-2}, 20 mA.cm^{-2}and 30 mA.cm^{-2}, respectively.

Fig. 9c and 9d represent the absorption bands as a function of time, and for two current densities. All profiles are similar, no additional band is observed in the various spectra, which means that no intermediate appears during the degradation process.

For a fixed time of degradation experiment, the ratios C_t/C_0 decrease linearly with the increasing current density: these linear variations could have been expected because of increasing surface reactions due to increasing current density. However, it is probable that due to the weak C_0 concentration and the limited current densities chosen in these experiments, no limit in surface reactions was reached.

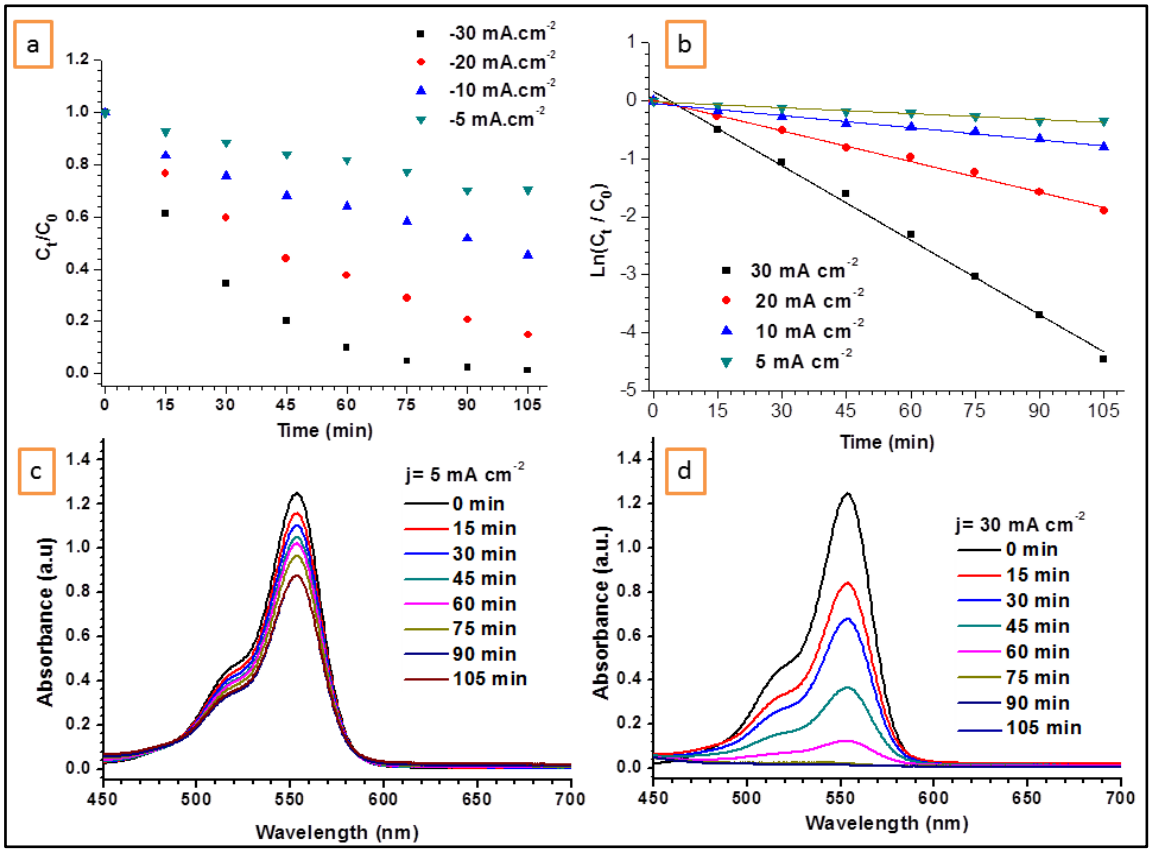

Figure 9. a) Degradation of RhB as a function of time, under different current densities; (b) Pseudo first-order kinetics of electrodegradation; (c) Variation of absorbance (UV absorption band at 554 nm) under a minimum current density of 5 mA.cm^{-2}; (d) under a maximum current density of 30 mA.cm^{-2}. (T = 25 °C, pH = 6.4).

Effect of concentration

The effect of the RhB concentrations varying between 5 and 20 mg. L^{-1} is shown in Fig. 10.

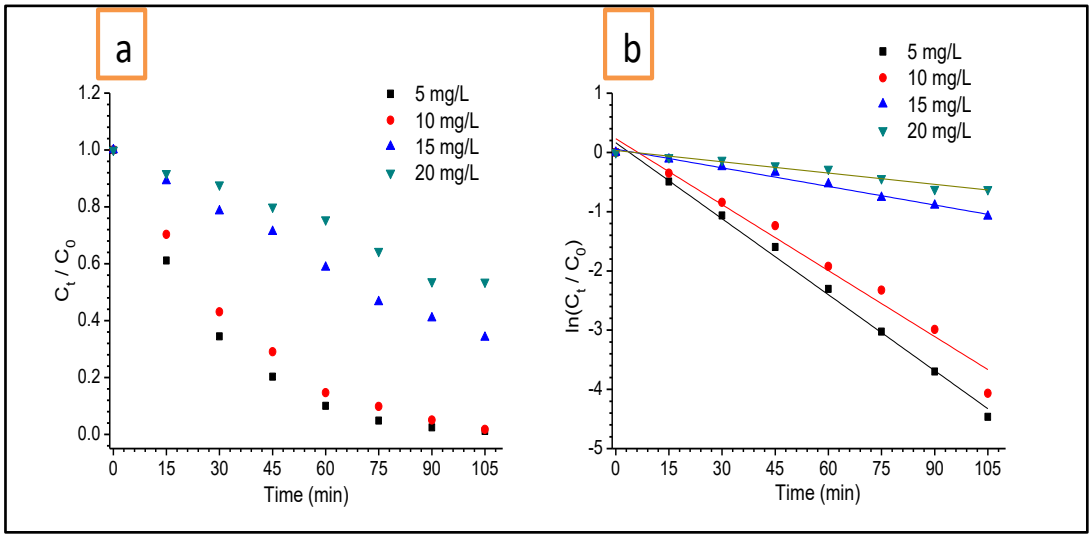

Figure 10. Effect of the initial concentration of RhB on the degradation process. (j= 30 mA.cm^{-2}, T = 25 °C, pH = 6.4)

The C_t/C_0 ratio for each concentration at the instant t decreases rapidly with concentration. We obtained a high catalytic efficiency for both concentrations 5 and 10 mg L^{-1}. This indicated an excellent anodic degradation which reached a rate of 98%. In addition, when we increased the concentration, the degradation rate was 65% and 46% for the concentrations 15 mg and 20 mg, respectively. The degradation kinetics could be described by the pseudo-first order kinetics model

as shown in Fig. 10b, with kinetic rate constants equal to k_5 = 0.0428 min^{-1}, k_{10} = 0.0371 min^{-1}, k_{20} = 0.0105 min^{-1} and k_{30}= 0.0064 min^{-1} for concentrations equal to 5 mg. L^{-1}, 10 mg. L^{-1}, 15 mg.L^{-1} and 20 mg.L^{-1}, respectively.
This strong decrease of concentration ratios C_t/C_0 with decreasing C_0 values, for a fixed working time t and a fixed current density, can be interpreted as follows:

• For low concentrations C_0, the reaction between RhB molecules and active species (e.g. OH°) at the electrode surface, via the HAp film, could be rapid, allowing a maximum of degradation of adsorbed RhB molecules;
• For high concentrations C_0, a saturation effect could occur at the interface electrode/solution, a limit in the exchanges would be reached, thus limiting the variation of C_t.

Conclusion

In this work, we were able to optimize the experimental conditions allowing the deposition of hydroxyapatite $Ca_{10}(PO_4)_6(OH)_2$ on stainless-steel substrates. We performed the electrodeposition of HAp on stainless-steel substrates, using the chronopotentiometric mode, in aqueous solutions of calcium nitrate tetrahydrate and dihydrogen phosphate. The optimized films of hydroxyapatite deposited on the stainless-steel substrate presented a remarkable electrocatalytic activity linked with their apparent porosity resulting from specific needle-like morphologies of HAp crystals. Several parameters (e.g. initial concentration of RhB) played an important role in the RhB degradation. The degradation mechanism followed a pseudo-first order kinetics law. In addition, the RhB UV absorption band decreased in intensity, without any modification in its profile, meaning that no intermediate appeared in the degradation process. In other terms, a direct mechanism of degradation was involved in these experiments. These HAp/SS electrodes can be considered as being promising for applications in the elimination of aquatic organic pollutants.

In this work, it can be noted that the HAp film thicknesses were not determined directly: however, calculated thicknesses allowed evaluating the thicknesses in the case on continuous dense layers. In fact, the main feature presently observed was the difference in the porosity of films deposited on SS substrate. This porosity induced by the anisotropic crystal growth of HAp grains in the film S3 could play a prominent role in the observed electroactivity, conditioned by exchanges “electron-active species” close to the SS surface and reinforced by the cavities in the films. The determination of thicknesses is planned to try to evaluate the porosity of these films.

Acknowledgments

This work was carried out in the framework of the PPR project financed by the CNRST under number PPR / 2015/32.

References

1 - D.F. Williams, On the mechanisms of biocompatibility, Biomaterials, **2008**, 29, 2941–2953.
2 - W. Cao, L.L. Hench, Bioactive materials, Ceram. Int., **1996**, 22, 493–507.
3 - L.L. Hench, Bioactive materials: The potential for tissue regeneration, J. Biomed. Mater. Res. **1998**, 41, 511–518.
4 - S. Jegannathan, T.S.N.S. Narayanan, K. Ravichandran, S. Rajeswari, Formation of zinc phosphate coating by anodic electrochemical treatment, Surf. Coatings Technol., **2006**, 200, 6014–6021.
5 - L. Kőrösi, I. Dékány, Preparation and investigation of structural and photocatalytic properties of phosphate modified titanium dioxide, Colloids Surfaces A Physicochem. Eng. Asp., **2006**, 280, 146–154.
6 - J. Ryu, K. Y. Kim, B. D. Hahn, J. J. Choi, W. H. Yoon, B. K. Lee, D. S. Park, C. Park, Photocatalytic nanocomposite thin films of TiO_2-β-calcium phosphate by aerosol-deposition, Catal. Commun., **2009**, 10, 596–599.
7 - B. León, Pulsed Laser Deposition of Thin Calcium Phosphate Coatings: Thin Calcium Phosphate Coatings Medical Implants; ed. by JA Jansen, B Leon, Springer: New York, **2009**, 101-155.
8 - U.M. Gross and D. Lassner, In Vitro and In Vivo Evaluation of Thin Calcium Phosphate Coatings: In Thin Calcium Phosphate Coatings Medical Implants: ed. by JA Jansen, B Leon, Springer: New York, **2009**, 67-99.
9 - H. Benhayoune, R. Drevet, J. Fauré, S. Potiron, T. Gloriant, H. Oudadesse, D. Laurent-Maquin, Elaboration of Monophasic and Biphasic Calcium Phosphate Coatings on Ti6Al4V Substrate by Pulsed Electrodeposition Current, Adv. Eng. Mater., **2010**, 12, B192-B199.
10 - R. Chakraborty, S. Sengupta, P. Saha, K. Das, S. Das, Synthesis of calcium hydrogen phosphate and hydroxyapatite coating on {SS316} substrate through pulsed electro-deposition, Mater. Sci. Eng. C, **2016**, 69, 875–883.
11 - N. Ben Jaber, R. Drevet, J. Fauré, C. Demangel, S. Potiron, A. Tara, A. Ben Cheikh Larbi, H. Benhayoune, A New Process for the Thermal Treatment of Calcium Phosphate Coatings Electrodeposited on Ti6Al4V Substrate, Adv. Eng. Mater., **2015**, 17, 1608–1615

12 - P. Arunachalam, M.N. Shaddad, A.S. Alamoudi, M.A. Ghanem, A.M. Al-Mayouf, Microwave-Assisted Synthesis of $Co_3(PO_4)_2$ Nanospheres for Electrocatalytic Oxidation of Methanol in Alkaline Media, Catalysts, **2017**, 7, 119.
13 - T. Liu, Y. Liang, Q. Liu, X. Sun, Y. He, A.M. Asiri, Electrodeposition of cobalt-sulfide nanosheets film as an efficient electrocatalyst for oxygen evolution reaction, Electrochem. Commun., **2015**, 60, 92-96.
14 - Q. Lu, K. Chen, W. Pan, X. Wu, K. Lu, Z. Xu, R. Liu, Room Temperature Electrodeposition of Ag_3PO_4 Films, J. Electrochem. Soc., **2016**, 163, D206–D211.
15 - M. Lefèvre, E. Proietti, F. Jaouen, J. P. Dodelet, Iron-Based Catalysts with Improved Oxygen Reduction Activity in Polymer Electrolyte Fuel Cells, Science, **2009**, 324, 71-74.
16 - G. C. Luque, J. L. Fernández, Electrocatalysis of oxygen reduction at electrodeposited molybdenum phosphate-based films, J. Power Sources, **2012**, 203, 57-64.
17 - R. Murugavel, A. Choudhury, M.G. Walawalkar, R. Pothiraja, C.N.R. Rao, Metal Complexes of Organophosphate Esters and Open-Framework Metal Phosphates: Synthesis, Structure, Transformations, and Applications, Chem. Rev., **2008**, 108, 3549-3655.
18 - K. Baďurová, O. Monfort, L. Satrapinskyy, E. Dworniczek, G. Gościniak, G. Plesch, Photocatalytic activity of Ag3PO4 and some of its composites under non-filtered and UV-filtered solar-like radiation, Ceram. Int., **2017**, 43, 3706-3712.
19 - X. Song, R. Li, M. Xiang, S. Hong, K. Yao, Y. Huang, Morphology and photodegradation performance of Ag_3PO_4 prepared by $(NH_4)_3PO_4$, $(NH_4)_2HPO_4$ and $NH_4H_2PO_4$, Ceram. Int., **2017**, 43, 4692-4701.
20 - Q. Li, Q. Zhang, H. Cui, L. Ding, Z. Wei, J. Zhai, Fabrication of cerium-doped lead dioxide anode with improved electrocatalytic activity and its application for removal of Rhodamine B, Chem. Eng. J., **2013**, 228, 806–814.
21 - X. Zhao, Y. Zhu, Synergetic Degradation of Rhodamine B at a Porous ZnWO4 Film Electrode by Combined Electro-Oxidation and Photocatalysis, Environ. Sci. Technol., **2006**, 40, 3367–3372.
22 - D.T.M. Thanh, P.T. Nam, N.T. Phuong, L.X. Que, N. Van Anh, T. Hoang, T.D. Lam, Controlling the electrodeposition, morphology and structure of hydroxyapatite coating on 316L stainless steel, Mater. Sci. Eng. C., **2013**, 33, 2037–2045.
23 - H. Benhayoune, R. Drevet, J. Faur, S. Potiron, T. Gloriant, H. Oudadesse, D. Laurent-Maquin, Elaboration of monophasic and biphasic calcium phosphate coatings on Ti6Al4V substrate by pulsed electrodeposition current, Adv. Eng. Mater., **2010**, 12, 192-199.
24 - S.D. Huelin, H.R. Baker, E.F. Merschrod S., K.M. Poduska, Phase-Selective Electroprecipitation of Calcium Phosphate Thin Films at Physiological Temperatures, Cryst. Growth Des., **2006**, 6, 2634-2636.
25 - M.C. Kuo, S.K. Yen, The process of electrochemical deposited hydroxyapatite coatings on biomedical titanium at room temperature, Mater. Sci. Eng. C., **2002**, 20, 153-160.
26 - A. Rakngarm, Y. Mutoh, Electrochemical depositions of calcium phosphate film on commercial pure titanium and Ti–6Al–4V in two types of electrolyte at room temperature, Mater. Sci. Eng. C., **2009**, 29, 275-283.
27 - Y. Han, K. Xu, J. Lu, Morphology and composition of hydroxyapatite coatings prepared by hydrothermal treatment on electrodeposited brushite coatings, J. Mater. Sci. Mater. Med., **1999**, 10, 243-248.
28 - A.K. Lynn, W. Bonfield, A Novel Method for the Simultaneous, Titrant-Free Control of pH and Calcium Phosphate Mass Yield, Acc. Chem. Res., **2005**, 38, 202-207.
29 - N. Eliaz, M. Eliyahu, Electrochemical processes of nucleation and growth of hydroxyapatite on titanium supported by real-time electrochemical atomic force microscopy, J. Biomed. Mater. Res. Part A., **2007**, 80, 621-634.
30 - C.A. Martinez-Huitle, S. Ferro, Electrochemical oxidation of organic pollutants for the wastewater treatment: direct and indirect processes, Chem. Soc. Rev., **2006**, 35, 1324-1340.
31 - S. Song, J. Fan, Z. He, L. Zhan, Z. Liu, J. Chen, X. Xu, Electrochemical degradation of azo dye C.I. Reactive Red 195 by anodic oxidation on Ti/SnO2–Sb/PbO2 electrodes, Electrochim. Acta., **2010**, 55, 3606-3613.
32 - G.F. Pereira, R.C. Rocha-Filho, N. Bocchi, S.R. Biaggio, Electrochemical degradation of bisphenol A using a flow reactor with a boron-doped diamond anode, Chem. Eng. J., **2012**, 198-199, 282-288.
33 - M. Tertis, M. Jitaru, M. Toma, Electrochemical treatment of nitrophenols containing wastewaters, Sci. Study Res., **2008**, IX, 281-292.
34 - T. Zeng, X. Yu, K. H. Ye, Z. Qiu, Y. Zhu, and Y. Zhang, BiPO4 film on ITO substrates for photoelectrocatalytic degradation, Inorg. Chem. Commun., **2015**, 58, 39–42.